Journal of Engineering and Technological Sciences

Research Paper

Analysis of the Effect of Permanent Magnet Width on Cogging Torque of Interior LSPMSM

Le Anh Tuan[1] & Nhu Y Do[2,*]

[1]Faculty of Energy Engineering, School of Electrical and Electronic Engineering, Hanoi University of Industry, No. 298 Cau Dien Street, Tay Tuu Ward, Hano, 100000, Vietnam
[2]Faculty of Electromechanics, Hanoi University of Mining and Geology, No.18 Vien Street - Dong Ngac Ward - Ha Noi, 100000, Vietnam

*Corresponding author: donhuy@humg.edu.vn

Abstract

The line-start synchronous permanent magnet synchronous motors have the advantages of high efficiency and line-starting capability. However, this type of motor has the drawback of high cogging torque, which is the main cause of vibration and noise during operation. Analyzing the factors affecting cogging torque is essential and important in the design of these motors. This paper studies the impact of magnet width on cogging torque. Theoretical analysis and finite element method simulations for the test motor show that the cogging torque can be significantly high, reaching up to 5% of the rated torque of the motor. Research results indicate that cogging torque can be reduced by decreasing the width of the permanent magnet. However, reducing the magnet width adversely affects the startup characteristics, torque, and efficiency of the motor, demonstrating the existence of an optimal width that balances cogging torque and other parameters in motor design. Additionally, the research results have been validated through experimental modeling, showing a close correlation in the shape of the cogging torque and the back eletromotive force characteristics, with a small error of less than 5%.

Keywords: *cogging torque; electric motor; line-start permanent magnet synchronous motor; permanent magnet; permanent magnet synchronous motor.*

Introduction

Today, the use of efficient energy-saving sources has become a strategy for every country around the world (Gerstlberger et al., 2014; Liu and Ren, 2020). Currently, electric energy accounts for a significant proportion, approximately 40% of total global energy consumption (Lin and Li, 2020). Among electric loads, electric motors are currently the most important and largest consumers in the industrial sector, consuming up to 45% of electric energy (Almeida et al., 2010; Saidur, 2010). Utilizing high-efficiency motors to replace low-efficiency ones is a very effective solution in the strategy for energy conservation. Among various types of motors, the line-start permanent magnet synchronous motor (LSPMSM) has advantages such as high efficiency, high power factor, high energy density, and self-starting capability (Ugale and Chaudhari, 2020; Anh-Tuan et al., 2016; Lin et al., 2020). Therefore, this type of motor is currently being researched and developed to partially replace the widely used squirrel-cage induction motors (Anh-Tuan et al., 2016; Lin and Li, 2020).

Although the LSPMSM has been confirmed to have many advantages, it also has cogging torque (CT) due to its nature as a permanent magnet synchronous motor (PMSM). This CT arises from the interaction between the permanent magnets (PM) of the rotor and the stator’s slots. The CT leads to relatively high vibration and acoutic noise levels during operation (Do et al., 2022; Zhao et al., 2019). These drawbacks are directly related to the motor's construction, particularly concerning the design of the permanent magnets (PMs) in the LSPMSM. Research to mitigate these disadvantages of the LSPMSM is currently a focus of various studies. In study (Behbahanifard and Sadoughi, 2016), the impact of magnet placement on CT was highlighted. The paper proposes a design solution using a magnet shifting method to reduce CT for a 4-pole LSPMSM. Simulation results using finite element analysis (FEA) method and experimental data show that the magnet shifting method is a very effective measure for reducing CT in the LSPMSM.

ISSN: 2337-5779
J. Eng. Technol. Sci. Vol. 58, No. 5, 2026, 697-713
DOI: 10.5614/j.eng.technol.sci.2026.58.5.8

Additionally, the research results indicate that this proposed method results in minimal iron core losses, with no change in the efficiency of the LSPMSM. In document (Jing et al., 2019), the influence of the number of poles and slots on CT was demonstrated. The paper proposes an analytical method that models the motor rotor as an equivalent magnetic motive force (MMF) distributed in the air gap (AG) to avoid the effects of rotor teeth and slots. Furthermore, calculations in the paper indicate that CT can be reduced by altering the number of stator slots.

Dosiek and Pillay (2007) and Gao, et al., (2017) research the impact of the positioning of PMs and the shifting of magnet blocks within the rotor of the LSPMSM to reduce harmonics and torque in the motor (Dosiek et al., 2007; Gao et al., 2017). From the results of study, two methods were proposed by Dosiek, et al., (2007) to reduce CT in PMSMs: magnet shifting and optimizing magnetic pole configurations. Simulation results indicate that CT can be nearly eliminated when using these two proposed methods. Besides, Gao, et al., (2017) describe a method to reduce CT in PMSM using the elementary-cogging-unit (ECU) approach. This proposed method was applied to motors with configurations of 12 slots/8 poles and 24 slots/8 poles. Results showed a reduction of 86.1% in CT for the 12-slot/8-pole machine and 95.5% for the 24-slot/8-pole machine. Additionally, the fundamental amplitude of the back electromotive force (B-EMF) waveform and the average value of the electromagnetic torque (ET) slightly decreased, but the THD index of the B-EMF waveform (B-EMF) and the ET ripple also showed a significant reduction. One of the key challenges in designing PMSM is to reduce CT (Abbaszadeh et al., 2011). In this research, the best shifting angles were determined to reduce CT using the method of design of experiments (DOE) in the design of the PMs.

On the other hand, the arrangement of the stator significantly affects CT (Dajaku and Gerling, 2014). The paper proposes a proposed stator design with shifted openings to the right and left to reduce CT and torque ripples in the motor. To demonstrate the effectiveness of the proposed method, the paper applies the design and optimization approach to two configurations of PMSM used in steering and traction applications. As a result, the simulation indicates that for the steering motor, the CT obtained is lower than 70 mNm with the new stator design. Additionally, a stepped slot-opening shift method is proposed to reduce CT in interior PMSMs (Zhao et al., 2019). The paper suggests segmenting the slot openings along the axis and shifting them by an optimal angle. The paper simulates an 8-pole, 12-slot interior permanent magnet motor (IPM), and the simulation results show that CT is reduced by 78.5%, 83.6%, and 95.4% for the 2-step, 3-step, and 5-step shifts, respectively.

Furthermore, the impact of flux barriers on CT in design was analyzed (Cao and Liu, 2020). The paper proposes two methods to reduce CT: optimizing the flux barrier design and the rotor slots. The research results indicate that both methods significantly reduce the effects of CT. The first method shows a reduction of 66.29% in CT, while the second method results in a 25% reduction. The influence of magnet size and flux barriers on CT was highlighted (Arehpanahi and Kashefi, 2018), leading to the proposal of the idea to segment the PM blocks and optimize the flux barrier design. The optimization process was conducted using the response surface method (RSM) as an appropriate technology. With the proposed optimal design, results showed that CT was decreased by 62% compared to the original standard design.

In other studies, the arrangement of the step-skew rotor also significantly affects CT (Luu et al., 2018). Based on the research results, the paper has identified suitable design parameters that can reduce CT in surface-mounted PMSM. Additionally, it was confirmed that the rotor step-skewing affects CT, indicating that significant reductions can be achieved by optimizing the number of rotor step skewing and the angle of the PM (Nian et al., 2019). However, changing the PM structure to a stepped inclination also results in a decrease in excitation torque and reluctance torque, which must be taken into consideration.

Summarizing the research results, cogging torque is an important issue in the design of LSPMSMs. Recent studies have focused on investigating the arrangement of PM bars, optimizing the number of magnetic poles, calculating the optimal PM placement angle or assessing magnetic flux barriers. However, no research has addressed how the width of the PM affects the cogging torque of the LSPMSM. Therefore, the content of this paper analysis the impact of PM width on cogging torque, as well as the relationship between changes in width to reduce cogging torque and other operating parameters of the LSPMSM. The application focus is on a LSPMSM rated at 2.2 kW, 380/220V, and $2p$=4. In this study, it is assumed that the configurations of the teeth, slots, magnetic circuit, windings, and squirrel cage of the stator and rotor remain unchanged, with the PMs made from NdFeB N40 type. The research employs theoretical analysis methods, followed by simulations using Ansys Maxwell to evaluate the CT in the LSPMSM. Additionally, some practical experiments in the laboratory will be conducted to validate the analysis results.

DOI: 10.5614/j.eng.technol.sci.2026.58.5.8

Methodology

Study Based on Analysis

In this section, the authors study the mathematical model and calculations related to the CT of LSPMSM based on analytical methods

Mathematical Model of LSPMSM

The mathematical model of the LSPMSM is expressed as follows, (Maraaba et al., 2018; Baradieh et al., 2018):

$$\begin{cases} u_{ds} = r_1 i_{ds} + \frac{d\Psi_{ds}}{d_t} - \omega_r \Psi_{qs} \\ u_{qs} = r_1 i_{qs} + \frac{d\Psi_{qs}}{d_t} + \omega_r \Psi_{ds} \end{cases} \tag{1}$$

$$\begin{cases} u'_{dr} = r'_{dr} i'_{dr} + \frac{d\Psi'_{dr}}{d_t} = 0 \\ u'_{qr} = r'_{qr} i'_{qr} + \frac{d\Psi'_{qr}}{d_t} = 0 \end{cases} \tag{2}$$

$$\begin{cases} \Psi_{ds} = (L_{ls} + L_{md}) i_{ds} + L_{md} i'_{dr} + \Psi'_m \\ \Psi_{qs} = (L_{ls} + L_{mq}) i_{qs} + L_{mq} i'_{qr} \end{cases} \tag{3}$$

$$\begin{cases} \Psi'_{dr} = L'_{lr} i'_{dr} + L_{md}(i_{ds} + i'_{dr}) + \Psi'_m \\ \Psi'_{qr} = L'_{lr} i'_{qr} + L_{mq}(i_{qs} + i'_{qr}) \end{cases} \tag{4}$$

where ω_r is the rotor angular velocity, Ψ'_m is the stator flux generated by the PMs, L_{ls} is the Leakage inductance of the stator winding, L_{md} and L_{mq} are the magnetizing inductances of d, q axes, i_{ds}, i_{qs}, i'_{dr}, i'_{qr} are the stator and current of d, q axes.

The ET of the LSPMSM is defined:

$$T_{el} = \frac{3}{2} p \left[\underbrace{(L_{md}.i'_{dr}.i_{qs} - L_{mq}.i'_{qr}.i_{ds})}_{T_{ind}} + \underbrace{\psi'_m.i_{qs}}_{T_{exc}} + \underbrace{(L_{md} - L_{mq}).i_{ds}.i_{qs}}_{T_{rel}} \right] \tag{5}$$

The ET:

$$T_{el} = T_{ind} + T_{exc} + T_{rel} \tag{6}$$

Additionally, the mechanical torque equation of the motor is:

$$J \frac{d\omega_m}{d_t} = T_{el} - T_L - B\omega_m \tag{7}$$

where T_e *and* T_L *are* electromagnetic and load torques; *B*, *J* are the friction coefficient, and moment of inertia.

Analysis of Cogging Torque of LSPMSM

In terms of structure, the LSPMSM motor is a hybrid design combining an asynchronous motor with additional PMs mounted on the rotor (Anh-Tuan, et al., 2016). In the design of the LSPMSM with 2*p*=4, various types of magnet structures can be used when integrated into the LSPMSM's rotor. This paper studies a typical LSPMSM with power 2.2 kW and 2*p*=4, featuring embedded rectangular magnets, as shown in Figure 1.

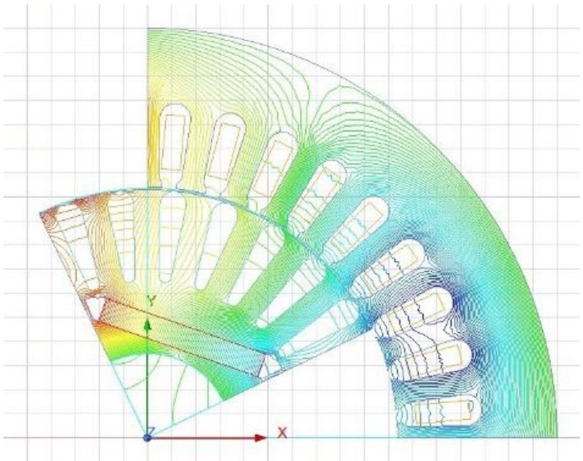

Figure 1 Configuration of LSPMSM 2.2kW, 2p=4.

The CT is the interaction between the PMs mounted on the rotor and the slots on the stator (Bianchini et al., 2012; Wan et al., 2022). The CT is defined:

$$T_{cog} = -\frac{\partial W(\alpha)}{\partial \alpha} \tag{8}$$

where $W(\alpha)$ is the magnetostatic energy of the motor. The position angle $\theta=0^0$ is defined as the center of a PM, and α is the angle between the centre position of the PM and that of a stator tooth. $W(\alpha)$ is defined:

$$W(\alpha) = \frac{1}{2\mu_0}\int B^2 dV \tag{9}$$

B is the flux density (FD) in the air gap (AG), therefore $W(\alpha)$ is determined (Zhang et al., 2010; Wang et al., 2003):

$$W(\alpha) = \frac{\int\left[B_r^2(\theta)\left(\frac{h_m}{h_m+\delta(\theta,\alpha)}\right)^2\right]dV}{2\mu_0} \tag{10}$$

where $B_r(\theta)$ is the distribution of the remanence of the PM in the AG as a function of angle θ, h_m is the PM's length in the direction of magnetization, and $\delta(\theta,\alpha)$ is the distribution of the effective AG length. $B^2_r(\theta)$ and $[h_m/(h_m+\delta(\theta, \alpha))]^2$ are periodic functions and will be analyzed as Fourier expansion. Thus, if $B^2_r(\theta)$ and $[h_m/(h_m+\delta(\theta, \alpha))]^2$ can be determined, it will be possible to calculate the energy $W(\alpha)$ from which the CT of the LSPMSM can be determined.

Fourier Expansion of B2r(θ)

The FD distribution $B_r(\theta)$ in the AG due to the remanence of the PM is shown in Figures 2 and 3. The analysis of $B^2_r(\theta)$ into Fourier expansion is as follows (Wang et al., 2003):

$$B_r^2(\theta) = B_{r0} + \sum_{n=1}^{\infty} B_{rn}\cos 2np\theta \tag{11}$$

where

$$B_{r0} = \alpha_p B_{0r}^2 \tag{12}$$

$$B_{rn} = \frac{2}{n\pi} B_{0r}^2 \sin(n\alpha_p\pi) \tag{13}$$

p is the number of pole pairs, B_{0r} is the amplitude of the FD in the AG generated by the remanence of PMs, and α_p is the pole arc coefficient of PM, as shown in Figure 2 below (Bianchini et al., 2012).

DOI: 10.5614/j.eng.technol.sci.2026.58.5.8

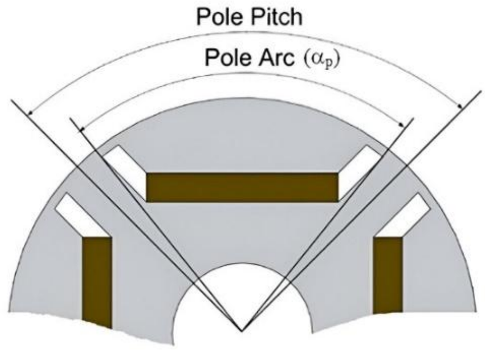

Figure 2 Pole pitch and pole arc (αp) of LSPMSM.

The distribution of magnetic FD $B_r(\theta)$ due to the remanence of the PM in the AG will be as shown in Figure 3.

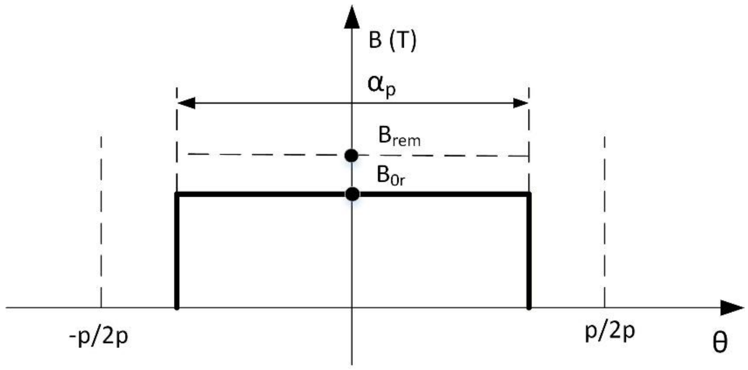

Figure 3 Distribution of magnetic FD $B_r(\theta)$ in air gap.

Fourier Expansion of $[h_m/(h_m+\delta(\theta, \alpha))]^2$

The LSPMSM has rotor and stator slots; therefore, $\delta(\theta,\alpha)$ is splited into the AG on the rotor and stator sides, denoted as $\delta_r(\theta,\alpha)$, $\delta_s(\theta,\alpha)$. The Fourier transform of $\delta(\theta,\alpha)$ is the superimposing of the Fourier expansion of $\delta_r(\theta,\alpha)$, $\delta_s(\theta,\alpha)$ (Wang et al., 2003).

$$\delta_s(\theta,\alpha) = \delta_{s0} + \sum_{n=1}^{\infty} \delta_{sn} \cos Z_1(\theta - \alpha) \tag{14}$$

$$\delta_r(\theta,\alpha) = \delta_{r0} + \sum_{n=1}^{\infty} \delta_{rn} \cos p\theta \tag{15}$$

The approximation of $[h_m/(h_m+\delta(\theta, \alpha))]^2$ can be calculated as:

$$\left(\frac{h_m}{h_m+\delta(\theta,\alpha)}\right)^2 \approx 1 - 1.646\,\frac{\delta_s(\theta,\alpha)+\delta_r(\theta,\alpha)}{h_m} + \left(\frac{\delta_s(\theta,\alpha)+\delta_r(\theta,\alpha)}{h_m}\right)^2 \tag{16}$$

Cogging Torque of the LSPMSM

From Eq. (11) and (16) substituted into (10), the Eq. (17) for the CT of the LSPMSM is determined (Zhang et al., 2010):

$$T_{cog} = \frac{Z_1 L_{Fe}(R_s^2 - R_r^2)}{8\mu_0 k_s} \cdot \begin{bmatrix} 2\left[\frac{2}{h_m^2}(\delta_{s0} + \delta_{r0}) - \frac{1.646}{h_m}\right] . \sum_{m=1}^{\infty} \delta_{sm} B_{r\frac{mZ_1}{2p}} \sin m k_s \pi \sin m\, Z_1 \left(\alpha + \frac{k_s \theta_{s1}}{2}\right) \\ + \frac{2}{h_m^2} \sum_{m=1}^{\infty} \delta_{sm} B_{r\frac{mZ_1}{2p}} \sin 2m k_s \pi \sin 2m\, Z_1 \left(\alpha + \frac{k_s \theta_{s1}}{2}\right) \\ + \frac{4B_{r0}}{h_m^2} \sum_{m=1}^{\infty} \delta_{sm} \delta_{r\frac{mZ_1}{2p}} \sin m k_s \pi \sin m\, Z_1 \left(\alpha + \frac{k_s \theta_{s1}}{2} - \beta_0\right) \\ + \frac{4}{h_m^2} \sum_{m=1}^{\infty} \sum_{n=1}^{\infty} \sum_{k=1}^{\infty} B_{rm}\, \delta_{sn} \delta_{rk} \sin \frac{2m k_s \pi}{Z_1} \sin 2m\, p \left(\alpha + \frac{k_s \theta_{s1}}{2}\right) \\ + (when: 2mp\ \pm nZ_1\ \pm kZ_1 = 0) \\ \frac{2}{h_m^2} \sum_{m=1}^{\infty} \sum_{n=1}^{\infty} \sum_{k=1}^{\infty} B_{rm}\, \delta_{sn} \delta_{rk} \sin n k_s \pi \sin \left(nZ_1 \alpha + nZ_1 \frac{k_s \theta_{s1}}{2} + kZ_2 \beta_0\right) \\ + (when: 2mp + \ nZ_1 + kZ_2 = 0\ or\ 2mp - \ nZ_1 - kZ_2 = 0) \\ \frac{2}{h_m^2} \sum_{m=1}^{\infty} \sum_{n=1}^{\infty} \sum_{k=1}^{\infty} B_{rm}\, \delta_{sn} \delta_{rk} \sin n k_s \pi \sin \left(nZ_1 \alpha + nZ_1 \frac{k_s \theta_{s1}}{2} - kZ_2 \beta_0\right) \end{bmatrix} \quad (17)$$

where *m* is the least common multiple of the number of stator slots and the number of *p*; Z_1, Z_2 are the number slots of stator and rotor; R_s and R_r are the inner radius of the stator and the outer radius of the rotor; L_{Fe} is the length of the stator, respectively.

Eq. (17) shows that cogging torque consists of a combination of high-order harmonics, exhibiting strong nonlinearity. This explains that the presence of cogging torque can cause significant vibrations and high noise levels in the LSPMSM, making it essential to minimize cogging torque in the design of the LSPMSM. Thus, considering the presence of T_{cog}, the mechanical torque Eq. (7) of the motor established in the LSPMSM's mathematical model will be modified as follows:

$$J \frac{d\omega_m}{d_t} = T_{el} + T_{cog} - T_L - B\omega_m \quad (18)$$

Eq. (18) shows the contribution of cogging torque in the torque formula, which differs from Eq. (7). This demonstrates that when cogging torque is significant, it will affect the electromechanical parameters (speed and torque of the motor). Since cogging torque is a function containing many high-order components, as indicated in Eq. (17), its presence will degrade the speed and torque characteristics, particularly leading to strong fluctuations.

Air Gap Flux Density

The paper utilizes the research results (Stoia et al., 2009) to determine the amplitude of the FD in the AG B_{0r} generated by the remanence of the PM in Eq. (12) and Eq. (13). In the calculations, the equivalent circuit diagram for the LSPMSM with 2*p*=4 without armature reaction is presented in Figure 4.

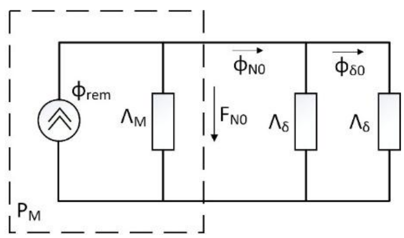

Figure 4 The equivalent circuit of the LSPMSM without armature reaction.

The operating characteristics of the PM shown in Figure 5.

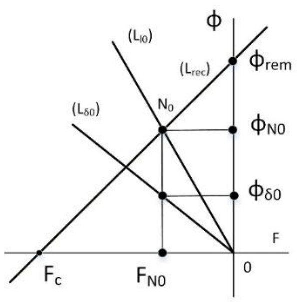

Figure 5 Determining of the operating point of the PM; (L_{rec}) – the recoil line of PM; (L_{l0}) - the load line without armature reaction; ($L_{\delta 0}$) – the AG load line.

DOI: 10.5614/j.eng.technol.sci.2026.58.5.8

The equations of the characteristic curves L_{rec} và L_{l0} are presented:

$$\Phi = \Phi_{rem} + \Lambda_M F \tag{19}$$

$$\Phi = -\Lambda_t F \tag{20}$$

Thus, the operating point of the PM N$_0$ (Φ_{N0}, F_{N0}) is determined as follows:

$$\Phi_{N0} = \Phi_{rem} \frac{\Lambda_t}{\Lambda_t + \Lambda_M} \tag{21}$$

$$F_{N0} = \frac{\Phi_{rem}}{\Lambda_t + \Lambda_M} \tag{22}$$

The the permeance of magnetic circuit is defined as:

$$\Lambda_t = \Lambda_\delta + \Lambda_\sigma = k_{\sigma M} . \Lambda_\delta \tag{23}$$

where Λ_δ is the permeance of the AG, representing the useful permeance corresponding to the useful flux circulating from the rotor through the AG to the stator. Λ_σ is the leakage permeance component, corresponding to the closed flux of each PM or the leakage flux through the stator slots, rotor, non-magnetic materials, and the AG between the magnet and the steel sheet.

The permeance of PM is defined as:

$$\Lambda_M = \frac{\mu_0 \mu_{rec} S_M}{h_m} \tag{24}$$

where S_M is the cross-sectional area of the PM, thus, the flux of the AG without armature reaction is determined as follows:

$$\Phi_{\delta 0} = \frac{\Lambda_\delta}{\Lambda_M / k_{\sigma M} + \Lambda_\delta} \Phi_{rem} \tag{25}$$

where the coefficient of the PM leakage $k_{\sigma M}$ is determined as

$$k_{\sigma M} = 1 + \frac{4 h_m}{\pi \mu_{re} \alpha_p \tau_p} \ln\left[1 + \frac{\pi \delta}{(1-\alpha_p)\tau_p}\right] \tag{26}$$

The permeance of AG gap Λ_δ is determined as:

$$\Lambda_\delta = (\alpha_p \tau_p L_{Fe} \mu_0)/(\delta k_C) \tag{27}$$

where τ_p is the pole pitch length, δ is the AG length, and k_C is Carter's coefficient. k_C is determined as k_C=k_{Cs}.k_{Cr} when there are slots in both the stator and rotor. k_{Cs} is determined:

$$k_{cs} = (\tau_{ss})/(\tau_{ss} - \gamma_s \delta) \tag{28}$$

$$\gamma_s = \frac{4}{\pi}\left[\frac{b_{Os}}{2\delta} arctg \frac{b_{Os}}{2\delta} - \ln\sqrt{1 + \left(\frac{b_{Os}}{2\delta}\right)^2}\right] \tag{29}$$

Thus, from Eq. (25), if we neglect the saturation, the flux of the AG without armature reaction is determined:

$$\Phi_{\delta 0} = \frac{\Phi_{rem}}{k_{\sigma M} + \mu_{rec} k_C \frac{C_\Phi}{C_p}} \tag{30}$$

where

$$C_\Phi = \frac{S_M}{S_p} \tag{31}$$

$$C_p = \frac{h_m}{\delta} \tag{32}$$

From Eq. (30), the FD of the AG B_{0r} without armature reaction can be calculated:

$$B_{0r} = \frac{B_{rem}}{k_{\sigma M} + \mu_{rec} k_c \frac{C_\Phi}{C_p}} \quad (33)$$

The back-electromotive force is determined as follows:

$$E_0 = 4.44 f w k_w \frac{\Phi_{rem}}{k_{\sigma M} + \mu_{rec} k_c \frac{C_\Phi}{C_p}} \quad (34)$$

From Eq. (12), (13) and (33), it is observed that the value and distribution of the FD in the AG are significantly influenced by the width of the magnet (α_p). Therefore, this leads to the CT generated in LSPMSM being affected as per Eq. (17). Additionally, Eq. (17) also indicates that the CT can be analysed into higher harmonic components, suggesting that when the width of the magnet changes, the level of harmonics and the ratio of harmonic components present in the CT also change. The analysis above demonstrates that the width of the magnet significantly affects the CT of the motor. Studying the extent of this influence will aid in improving the design quality of LSPMSMs.

Study Based on Simulation

The experimental LSPMSM with the specifications: 2.2 kW, 2*p*=4, voltage 380/220V is used to evaluate the influence of the width of the PM on CT. Detailed parameters of the motor are presented in Table 1.

Table 1 LSPMSM parameters

Parameters	Symbol	Value	Unit
Stator outer diameter	D_{in}	245	mm
Stator inner diameter	D_{out}	152	mm
Rotor outer diameter	D'	151	mm
Rotor shaft diameter	D_t	52	mm
Stator steel material	*Steel 1008*		
Number of stator slots	Z_1	36	slots
Number of rotor slots	Z_2	28	slots
Air gap length	δ	0,5	mm
Power supply voltage	U_n	380/220	VAC
Power supply frequency	f	50	Hz
Magnet material		NdFeB-N40	
Magnet dimensions	$l_M \times h_M \times w_M$	70 x 5 x 33	mm

Ansys/Maxwell software is applied to simulate, analyse, and evaluate the characteristics and parameters of the experimental LSPMSM motor in Table 1. The model of the 2.2 kW LSPMSM is simulated as shown in Figure 6.

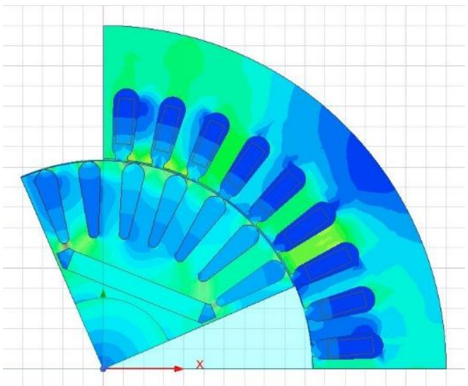

Figure 6 LSPMSM model of 2.2kW, 4p in simulation.

Furthermore, in this paper the simulation scenario involves changing the dimensions of the PM to assess the influence of the width of the PM (w_M) on the CT of the LSPMSM. The preliminary calculated width of the magnet is w_M=33mm (Table 1), with the maximum PM width occurring when the PM fully occupies the rectangular slot (Figure 6), $w_{M.max}$=35mm. Reducing the width will decrease the coverage area of the PM on the rotor surface, thereby reducing the induced B-EMF of the LSPMSM as well as the magnetic field strength generated by the PM. Therefore, to ensure symmetrical increases and decreases in the PM width on both sides, the width of the PM is varied in the range of w_M=31 to 35mm with an adjustment step of 1 mm.

DOI: 10.5614/j.eng.technol.sci.2026.58.5.8

Results

The paper conducts analytical calculations, simulations, and laboratory experiments on several characteristics and operating parameters of the motor to evaluate the impact of the width of the PM on CT. The results of the calculations, simulations, and experiments are as follows:

Simulation Results

The model of the 2.2 kW motor in Ansys/Maxwell constructed above is used. The CT and several characteristics of the motor are simulated. Some simulation results with Ansys/Maxwell applying the FEA method are shown below:

Speed Characteristics

The LSPMSM's speed characteristics during the simulation are shown in Figure 7.

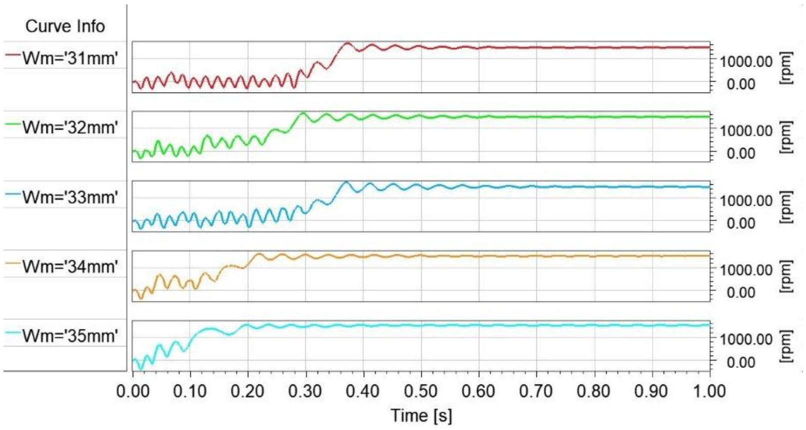

Figure 7 Speed characteristics of LSPMSM 2.2kW, 2p=4.

The results in Figure 7 show that when the width of the PM w_M changes from 31 mm to 35 mm, the LSPMSM can start under rated load. The starting characteristics of the LSPMSM improve as the width of the magnet increases. An investigation of the starting parameters of the LSPMSM motor based on the width of the PM is presented in Table 2 below.

Table 2 Parameters for evaluating the speed characteristics.

w_M (mm)	Transient time t_{ts} (s)	Speed deviation $\Delta\omega$ (rpm)
31	1.23	1
32	1.26	2
33	1.11	4
34	1.12	6
35	1.12	9

The results in Table 2 indicate that among the surveyed dimensions, the best starting characteristics correspond to a PM width of w_M = 33 mm. When the width is reduced, the starting time increases, and the amplitude of oscillation decreases; conversely, when the width is increased, both the starting time and frequency deviation increase. This can be explained by the fact that changing the width of the PM leads to an increase in the magnetic flux density in the AG, as described by Eq. (33). Reducing the width of PM decreases the magnetic flux density, resulting in a reduction of the excitation torque, as stated in Eq. (6) and (18), making it difficult for the LSPMSM to synchronize. Conversely, increasing the width of the PM leads to an increase in CT, as indicated in Eq. (17), which adversely affects the starting characteristics, as shown in Eq. (18).

Air Gap Flux Density Distribution

The simulation results of the FD distribution in the AG, generated by remanence the PM without armature reaction, are shown in Figure 8 below.

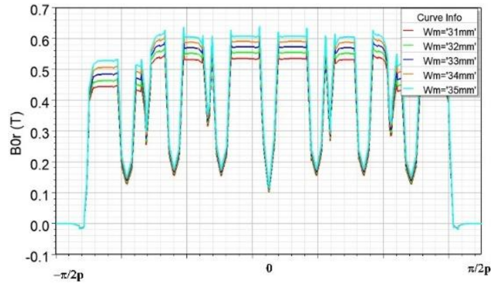

Figure 8 The FD distribution in the AG.

From Figure 8, the distribution of $B_{0r}(\theta)$ is influenced by the stator and rotor slots, thus the distribution $B_{0r}(\theta)$ is not flat as shown in Figure 3. The average value of $B_{0r}(\theta)$ in the range α_p is determined between the simulation with FEM and the analytical calculations in section 3.3, using the motor parameters in Table 1 and different values of w_M as shown in Table 3 below.

Table 3 Analytical calculation and simulation values B_{0r}.

w_M (mm)	Analytical calculation B_{0r} (T)	FEM simulation B_{0r} (T)	Error $\Delta E\%$
31	0.405	0.4027	5.7
32	0.420	0.4178	5.2
33	0.450	0.4326	3.9
34	0.471	0.4473	5.0
35	0.480	0.4619	6.8

From Table 3, it can be observed that in the range α_p , the analytical calculation and simulation of FD distributions are equivalent. The maximum error occurs when w_M=35mm, where the discrepancy between the two methods is largest, reaching a value of 6.8%. Thus, it can be concluded that the analytical calculation method as in Eq. (33) and the simulation are comparable, with the error being at an acceptable level.

Phase Back-EMF

With different values of w_M, the simulation results of the phase B-EMF are shown in Figure 9 below.

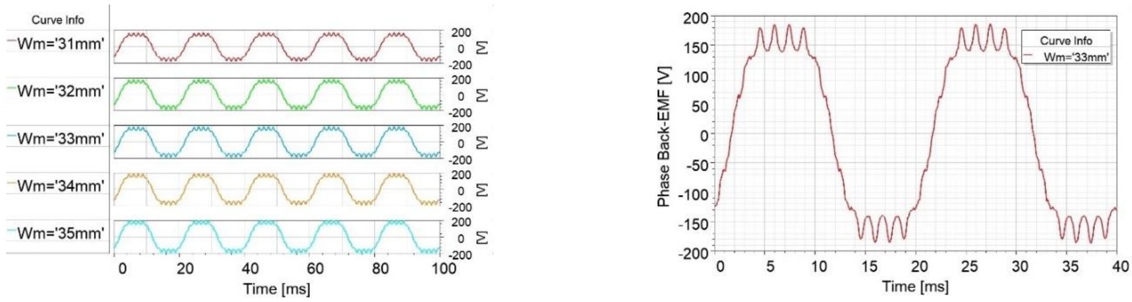

(a) (b)

Figure 9 Phase B-EMF of LSPMSM 2.2kW, $2p$=4: (a) composite characteristic graph and (b) single characteristic graph with w_M=33mm.

The simulated waveform of the B-EMF of the motor is not sinusoidal in Figure 9, but has got a head flap that contain sawtooth shapes. This is due to the magnetic field primarily passing through the stator teeth of the motor, which affects the magnetic field passing through the stator windings. The FFT analysis of the B-EMFW shows the harmonic components of the LSPMSM, as shown in Figure 10.

DOI: 10.5614/j.eng.technol.sci.2026.58.5.8

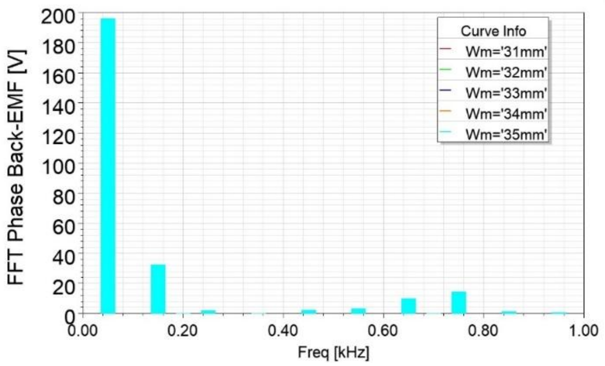

Figure 10 FFT analysis of phase B-EMFW of LSPMSM.

In Figure 10, the B-EMFW contains many odd-order harmonic components. Notably, the significant harmonic components in this case are the 3rd, 13th, and 15th orders. The total harmonic distortion (THD) index is utilized to assess the harmonics of the B-EMF. In addition to the THD index, *ΔE%* is the deviation index between the fundamental amplitude of the waveform and the rated phase voltage of the power supply, which is used to evaluate the B-EMF of the LSPMSM (Do et al., 2024).

$$\Delta E\% = \left|\frac{E_{1NB}-220}{E_{1NB}}.100\%\right| \quad (35)$$

where E_{1NB} is the rms of the no-load electromotive force of the fundamental waveform. The results of the FFT analysis of the harmonic components are provided in Table 4.

Table 4 FFT analysis of the harmonic components of the B-EMFWs.

w_M (mm)	1st	3rd	13th	15th	THD	ΔE%
31	172.2	26.7	8.8	12.1	18.2	27.9
32	178.4	28	9.1	12.8	18.4	23.5
33	184.45	29.4	9.4	13.5	18.6	19.5
34	190.4	30.9	9.8	14.2	18.9	15.8
35	196.2	32.6	10.1	14.9	19.4	12.2

The results in Table 4 show that as the width of the PM increases, the THD of the B-EMFW shows a slight upward. Correspondingly, the harmonic components of the 3rd, 13th, and 15th orders also increase. However, it can also be observed that as w_M increases, the amplitude of the fundamental waveform increases significantly, leading to a rapid decrease in the voltage deviation of the fundamental B-EMF *ΔE%* dropping from 27.9% at w_M=31mm to 12.2% at w_M=35 mm. This is entirely consistent with the theory presented in Eq. (34).

Cogging Torque Characteristics

The simulation results of the CT for the 2.2 kW LSPMSM with different w_M according to the simulation scenario are shown in Figure 11.

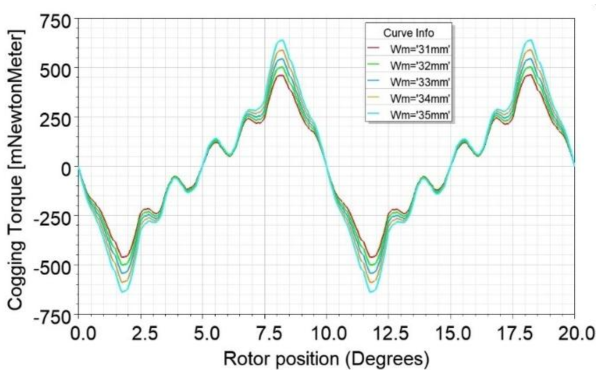

Figure 11 The CT versus mechanical degrees.

The CT exhibits a periodic cycle corresponding to one tooth of the stator (equivalent to 10^0 with a stator having 36 slots) in Figure 10. The FFT analysis of the CT waveform yields the results shown in Figure 12.

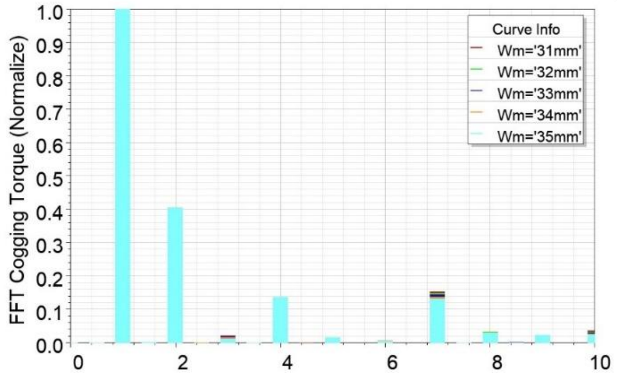

Figure 12 FFT expansion of CT wave.

In addition to the amplitude of the fundamental waveform with frequency f_1, the CT contains many harmonic components that are multiples of the fundamental frequency in Figure 12. It can also be observed in Figure 12 that the harmonics of orders 2nd, 4th, and 7th have significant amplitudes. The research results on CT when varying the magnet width of the LSPMSM are presented in Table 5 below.

Table 5 FFT expansion of CT.

w_M (mm)	1st (mNm)	2nd (mNm)	4th (mNm)	7th (mNm)
31	324	114	38	50
32	349	127	42	52
33	375	140	47	54
34	402	157	53	56
35	431	176	59	57

The width of the PM w_M varies from 31 mm to 35 mm, which causes the amplitude of the CT to change and gradually increase with the width of the magnet. The maximum amplitude of the CT is relatively high, peaking when w_M=35mm, at which point the peak value of the CT reaches 0.68 Nm. This maximum amplitude reaches 5% compared to the rated torque of the motor (14 Nm). Additionally, besides the fundamental component in the CT, there are many components that are integer multiples of the fundamental frequency (including both even and odd multiples), which is fully consistent with the theoretical basis analysed in Eq. (17) above.

Electromagnetic Torque

The simulation results of the ET for the LSPMSM 2.2 kW are shown in Figure 13.

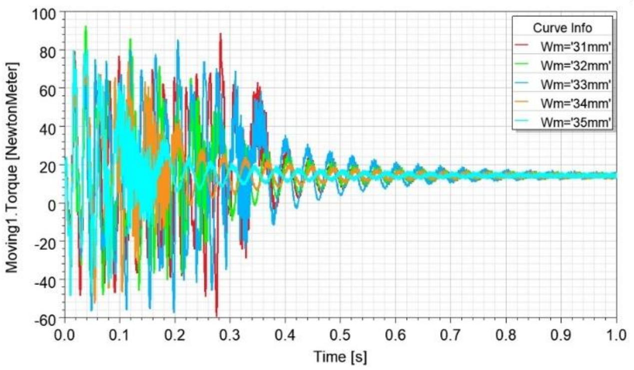

Figure 13 The ET of LSPMSM.

Thus, in the steady state mode with the characteristics of the electromagnetic force shown in Figure 13, the LSPMSM operates unstably. At this point, the ET of the LSPMSM oscillates around the rated torque. To assess the level of torque ripple, some studies use the torque ripple coefficient k. The coefficient is defined through the values of maximum

DOI: 10.5614/j.eng.technol.sci.2026.58.5.8

torque, minimum torque, and average torque. In summary, the formula is used for calculating the torque ripple factor in the study as follows (Song et al., 2020):

$$k = \frac{T_{max} - T_{min}}{T_{avg}} \quad (36)$$

where T_{max}, T_{min}, T_{avg} represent the maximum, minimum and average value of torque respectively. Summary of the calculated torques of the LSPMSM for different w_M values is presented in Table 6 below.

Table 6 Calculation of k for evaluating the working torque.

w_M (mm)	T_{max}	T_{min}	Torque ripple coefficient k
31	16.2	12.2	0.285
32	16.5	12.2	0.307
33	16.9	11.9	0.357
34	16.4	11.3	0.364
35	16.3	11.1	0.378

When w_M increases, the coefficient k also increases, as shown in Table 6. That is in this case, an increase in w_M leads to a greater level of fluctuation in the ET during steady-state operation. This can be explained by the fact that CT is one of the additional torques that significantly affects the ET of the motor. Moreover, it was noted that the amplitude of the CT reaches its maximum value at w_M=35 mm, meaning that the level of fluctuation in the ET caused by CT will be at its highest. Additionally, it can be found that when operating in steady-state with different w_M values, the LSPMSM exhibits a very high amplitude of ET fluctuation (over 28.5%). This can be explained by the presence of CT components, which contain many high-order harmonics as described in Eq. (17). This will cause significant fluctuations in the electromagnetic torque of the LSPMSM, as shown in Eq. 18. As the cogging torque increases, the level of fluctuations also increases, thus the simulation results are entirely consistent with the theoretical results established.

Efficiency Characteristics

Efficiency characteristics of the LSPMSM in steady-state operation as shown in Figure 14.

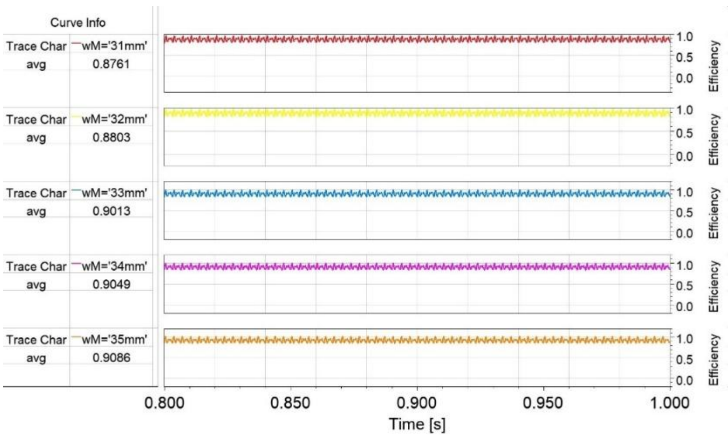

Figure 14 Efficiency of LSPMSM 2.2kW, 2p=4.

The efficiency of the motor remains high with varying values of the w_M as shown in Figure 14. When compared to the energy efficiency standard IEC/EN 60034-30-1 on efficiency classes of line operated AC motors, the LSPMSM with $w_M \geq$ 33 mm meets the IE4 standard ($\eta \geq$ 89.5%). The other two cases of the LSPMSM meet the IE3 standard ($\eta \geq$ 86.7%).

Experimental Results

The authors fabricated a 2.2 kW, 2p=4 LSPMSM for experimental purposes. In this experimental LSPMSM, the authors used PMs with w_M=33 mm. The team also established a measurement and testing model for the motor based on the schematic shown in Figure 15 to measure the experimental parameters of the LSPMSM.

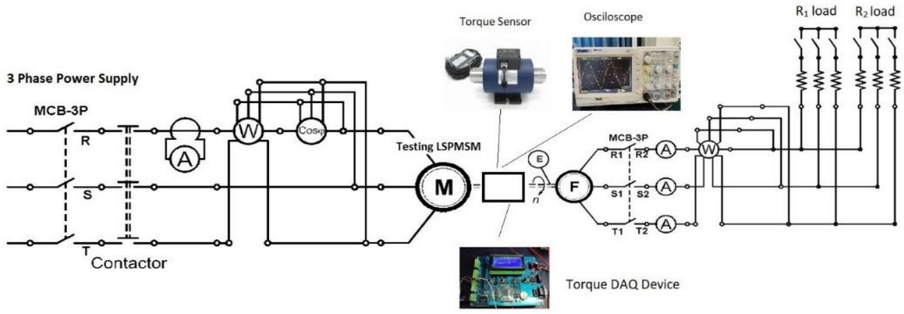

Figure 15 Schematic diagram of the LSPMSM testing.

The ZHKY901 torque sensor is used to measure the shaft torque. This torque sensor is mounted coaxially with the experimental LSPMSM. A torque DAQ device is utilized in the measurement model. This device is capable of processing data collected from the torque sensor, handling data, and transmitting it to a computer. Additionally, a Protek 5060 oscilloscope is used, connected to the outputs of the sensors to measure the waveform of signals such as current, voltage, etc.

Cogging Torque

The CT of the experimental motor is measured using the ZHKY901 sensor, with data collected and processed through the torque DAQ device. By varying the rotor's rotation angle when not powered, the sensor and DAQ device record the values of the shaft torque. These measured values correspond to the CT at different rotation angles. Additionally, based on the experimental schematic in Figure 15, the research team installed the LSPMSM, sensors, and measurement devices for the experiment. The experiment to measure CT was conducted in the laboratory as shown in Figure 16.

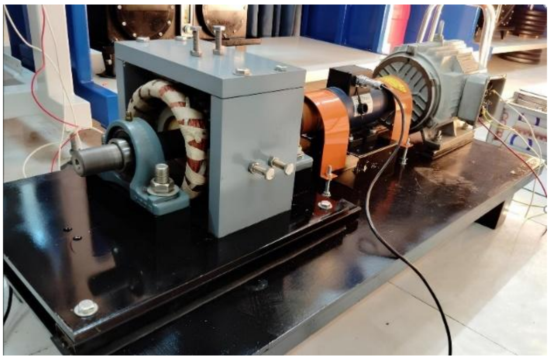

Figure 16 Testing CT of LSPMSM.

The results of the CT measurements from the LSPMSM experiment are presented in Figure 17

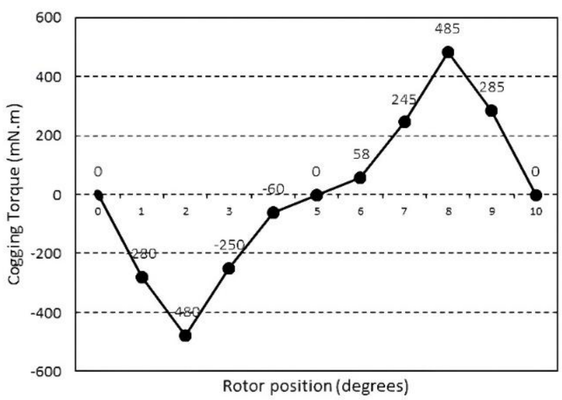

Figure 17 Experimental CT versus rotor position.

There is a similarity in the shape of the CT characteristics between the experimental and simulated data shown in Figure 11, as illustrated in Figure 17. The error margin between the experimental and simulated CT is ΔT_{cog} = 5%. However, the

DOI: 10.5614/j.eng.technol.sci.2026.58.5.8

simulated characteristics in Figure 11 display distinct peaks and valleys of the CT, which are not observed in the experimental data. This discrepancy is consistent with the fact that during the experimental process, only discrete parameters could be measured.

Testing Phase Back-EMF

In the study, the paper also experimentally measures the B-EMFW of the LSPMSM. The experimental LSPMSM is connected to a secondary motor, which is a synchronous motor operating at a speed of 1,500 rpm. At this point, the experimental LSPMSM functions as a generator, although its output is left open-circuit. The voltage waveform measured at the terminals of the experimental LSPMSM will represent the B-EMF. The waveform of the B-EMF of the LSPMSM is measured and displayed using the Protek 5060 oscilloscope. The experimental results of the B-EMF are shown in Figure 18 below

Figure 18 Phase B-EMF of testing LSPMSM.

The waveform of the B-EMF of the LSPMSM is not sinusoidal; it has a flat head shape and exhibits a sawtooth appearance due to the influence of the tooth and stator slot configuration, as seen in Figure 16. The error margin of the B-EMF between the experimental and simulated results is ΔE=4%, indicating a good agreement between theory and experiment when studying the effect of magnet width on the parameters of the LSPMSM.

Discussion

This paper discusses the impact of the width of the PMs on CT, as well as other characteristics and operating parameters of the LSPMSM with $2p$=4. The results of the theoretical analysis demonstrate the presence of CT in the mathematical equation describing the torque of the LSPMSM, as indicated in Eq. (18). The research results also indicate that CT can be reduced by decreasing the width of the PMs. However, reducing the width may lead to increases in certain parameters and characteristics, such as starting performance, B-EMF, efficiency, and torque ripple. The simulation results using FEA for the LSPMSM rated at 2.2 kW and $2p$=4, with magnet widths varying from 31 mm to 35 mm, indicate that the CT can reach significant values, potentially up to 5% of the rated torque at w_M=35mm, this leads to increased vibration and acoustic noise levels in the LSPMSM.

The paper also conducted experiments on the CT and B-EMF parameters of the LSPMSM, 2.2kW, $2p$=4, the experimental results indicate a similarity in the characteristic shapes of CT and B-EMFW between the experimental and simulated results, with an error of ΔT_{cog}=5% for the CT characteristics and $\Delta E\%$=4% for the B-EMF characteristics. This demonstrates a good agreement between theory and experiment when studying the effect of magnet width on the parameters of the LSPMSM.

In summary, the paper essentially investigates the influence of PM size on CT. The paper combines theoretical research on CT with the application of FEA software for simulation to validate the theoretical analysis. Finally, a prototype of LSPMSM is tested to confirm the accuracy of the CT simulation results. From the research results, some conclusions regarding PM sizes are drawn in the design to minimize CT during operation.

Conclusion

For PM motors in general and LSPMSMs in particular, one of the main drawbacks is the presence of CT, which arises from the interaction between the PMs attached to the rotor and the slots on the stator. Recent studies have focused on investigating the arrangement of PM bars, optimizing the number of PM poles, determining the optimal PM placement angle, or calculating magnetic flux barriers. However, there has been no research addressing how the width of the PM affects the CT of the LSPMSM. In addition to CT, the paper also highlights the impact of magnet width on other operating parameters of the LSPMSM, such as speed characteristics, B-EMF characteristics, and efficiency. The simulation results demonstrate a significant influence of magnet width on these parameters.

Additionally, the research findings of this paper also demonstrate that reducing the width of the magnet can decrease CT, but it adversely affects other operating characteristics of the LSPMSM. This indicates the existence of an optimal width value of PM that minimizes CT while still allowing for the selection of other suitable parameters. This will be the focus of further research on this issue regarding the selection of optimal dimensions of PMs in LSPMSM design.

Compliance with ethics guidelines

The authors declare they have no conflict of interest or financial conflicts to disclose.

This article contains no studies with human or animal subjects performed by the authors.

References

Abbaszadeh, K., Alam, F. R., & Saied, S. A. (2011). Cogging torque optimization in surface-mounted permanent-magnet motors by using design of experiment. *Energy Conversion and Management*, *52*(10), 3075–3082. https://doi.org/10.1016/j.enconman.2011.04.009

Anh-Tuan, L., Duc-Hung, B., & Anh-Tuan, P. (2016). Saturable q-axis magnetizing inductance calculation of line start-permanent magnet synchronous motors using lumped parameter mode. In *2016 IEEE International Conference on Sustainable Energy Technologies (ICSET)* (pp. 364–368). IEEE. https://doi.org/10.1109/ICSET.2016.7811811

Arehpanahi, M., & Kashe, H. (2018). Cogging torque reduction of interior permanent magnet synchronous motor (IPMSM). *Tc*, *50*(4), 0. *Scientia Iranica, 25*(3), 1471–1477. https://doi.org/10.24200/sci.2017.4365

Baradieh, K., Al-Hamouz, Z., & Abido, M. (2018). ANN based broken rotor bar fault detection in LSPMS motors. *J Electr Electron Syst*, *7*(273), 2332–0796. https://doi.org/10.3390/machines7010004

Behbahanifard, H., & Sadoughi, A. (2016). Cogging torque reduction in line start permanent magnet synchronous motor. *Journal of Electrical Engineering and Technology*, *11*(4), 878–888. https://doi.org/10.5370/JEET.2016.11.4.878

Bianchini, C., Immovilli, F., Lorenzani, E., Bellini, A., & Davoli, M. (2012). Review of design solutions for internal permanent-magnet machines cogging torque reduction. *IEEE Transactions on Magnetics*, *48*(10), 2685–2693. https://doi: 10.1109/TMAG.2012.2199509

Cao, Z., & Liu, J. (2020). Cogging torque reduction for outer rotor interior permanent magnet synchronous motor. In *IECON 2020 The 46th Annual Conference of the IEEE Industrial Electronics Society*, 2689–2693. IEEE. https://doi.org/10.1109/IECON43393.2020.9254887

Dajaku, G., & Gerling, D. (2014). New methods for reducing the cogging torque and torque ripples of PMSM. In *2014 4th International Electric Drives Production Conference (EDPC)*, 1–7. IEEE. https://doi.org/10.1109/EDPC.2014.6984396

De Almeida, A. T., Ferreira, F. J., & Fong, J. A. (2010). Standards for efficiency of electric motors. *IEEE Industry Applications Magazine*, *17*(1), 12–19. https://doi.org/10.1109/MIAS.2010.939427

Do, N. Y., Le, T. A., & Ngo, X. C. (2022). Effect of Permanent Magnet Structure on The Performance of LSPMSM with a Power of 22 kW and 3000 rpm. In *IOP Conference Series: Earth and Environmental Science*, *1111*(1), 012047. IOP Publishing. https://doi.org/10.1088/1755-1315/1111/1/012047

Do, N. Y., Thuy, T. B., & Cuong, N. X. (2024). Rotor Configuration for Improved Working Characteristics of Lspmsm in Mining Applications. *Natsional'nyi Hirnychyi Universytet. Naukovyi Visnyk*, (3), 79–86. https://doi.org/10.33271/nvngu/2024-3/079

Dosiek, L., & Pillay, P. (2007). Cogging torque reduction in permanent magnet machines. *IEEE Transactions on industry applications*, *43*(6), 1565–1571. https://doi.org/10.1109/IAS.2006.256518

Gao, J., Wang, G., Liu, X., Zhang, W., Huang, S., & Li, H. (2017). Cogging torque reduction by elementary-cogging-unit shift for permanent magnet machines. *IEEE Transactions on Magnetics*, *53*(11), 1–5. https://doi.org/10.1109/TMAG.2017.2712799

Gerstlberger, W., Præst Knudsen, M., & Stampe, I. (2014). Sustainable development strategies for product innovation and energy efficiency. *Business Strategy and the Environment*, *23*(2), 131–144. https://doi.org/10.1002/bse.1777

Jing, L., Gong, J., & Lin, Y. (2019). Analysis and reduction of cogging torque of line-start permanent magnet motors. *Progress In Electromagnetics Research M*, *78*, 115–124. https://doi.org/10.2528/PIERM18120902

Lin, B., & Li, Z. (2020). Is more use of electricity leading to less carbon emission growth? An analysis with a panel threshold model. *Energy Policy*, *137*, 111121. https://doi.org/10.1016/j.enpol.2019.111121

DOI: 10.5614/j.eng.technol.sci.2026.58.5.8

Lin, M., Li, D., Zhao, Y., Ren, X., & Qu, R. (2020). Improvement of starting performance for line-start permanent magnet motors by winding reconfiguration. *IEEE Transactions on Industry Applications*, *56*(3), 2441–2450. https://doi.org/10.1109/TIA.2020.2968277

Liu, Q., & Ren, J. (2020). Research on the building energy efficiency design strategy of Chinese universities based on green performance analysis. *Energy and Buildings*, *224*, 110242. https://doi.org/10.1016/j.enbuild.2020.110242

Luu, P. T., Lee, J. Y., Hwang, W., & Woo, B. C. (2018). Cogging torque reduction technique by considering step-skew rotor in permanent magnet synchronous motor. In *2018 21st International Conference on Electrical Machines and Systems (ICEMS)*, 219–223. IEEE. https://doi.org/10.23919/ICEMS.2018.8549086

Maraaba, L., Al-Hamouz, Z., Milhem, A., & Abido, M. (2018). Modelling of interior-mount LSPMSM under asymmetrical stator winding. *IET Electric Power Applications*, *12*(5), 693–700. https://doi.org/10.1049/iet-epa.2017.0525

Nian, S., Zhu, L., Luo, X., & Huang, Z. (2019). Analytical methods for optimal rotor step-skewing to minimize cogging torque in permanent magnet motors. In *2019 22nd International Conference on Electrical Machines and Systems (ICEMS)*, 1–5. IEEE. https://doi.org/10.1109/ICEMS.2019.8921502

Saidur, R. (2010). A review on electrical motors energy use and energy savings. *Renewable and sustainable energy reviews*, *14*(3), 877–898. https://doi.org/10.1016/j.rser.2009.10.018

Song, S., Fang, G., Hei, R., Jiang, J., Ma, R., & Liu, W. (2020). Torque ripple and efficiency online optimization of switched reluctance machine based on torque per ampere characteristics. *IEEE Transactions on Power Electronics*, *35*(9), 9608–9616. https://doi.org/10.1109/TPEL.2020.2974662

Stoia, D., Cernat, M., Jimoh, A. A., & Nicolae, D. V. (2009). Analytical design and analysis of line-start permanent magnet synchronous motors. In *AFRICON 2009*, 1–7. IEEE. https://doi.org/10.1109/AFRCON.2009.5308177

Ugale, R. T., & Chaudhari, B. N. (2020). Performance enhancement of line start permanent magnet synchronous motor with a special consequent pole rotor. *IEEE Transactions on Energy Conversion*, *36*(3), 1972–1982. https://doi.org/10.1109/TEC.2020.3038725

Wan, X., Yang, S., Li, Y., Shi, Y., & Lou, J. (2022). Minimization of cogging torque for V-type IPMSM by the asymmetric auxiliary slots on the rotor. *IEEE Access*, *10*, 89428-89436. https://doi.org/10.1109/ACCESS.2022.3201246

Wang, X., Yang, Y., & Fu, D. (2003). Study of cogging torque in surface-mounted permanent magnet motors with energy method. *Journal of Magnetism and Magnetic Materials*, *267*(1), 80–85. https://doi.org/10.1016/S0304-8853(03)00324-X

Zhang, B. Y., Cui, G., Wang, S., & Feng, G. H. (2010). Study of cogging torque in line-start PMSM with proper fractional slot winding. In *2010 International Conference on E-Product E-Service and E-Entertainment*, 1–4. IEEE. https://doi.org/10.1109/ICEEE.2010.5660985

Zhao, J., Wang, J., Zhou, L., Huang, W., Ma, Y., & Zhang, Z. (2019). Cogging torque reduction by stepped slot-opening shift for interior permanent magnet motors. In *2019 22nd International Conference on Electrical Machines and Systems (ICEMS)*, 1–4. IEEE. https://doi.org/10.1109/ICEMS.2019.8921448

Zhao, Y., Li, D., Lin, M., & Qu, R. (2019). A novel dual stator line-start permanent magnet synchronous machine. In *2019 IEEE International Electric Machines & Drives Conference (IEMDC)* (pp. 1526–1531). IEEE. https://doi.org/10.1109/IEMDC.2019.8785230

Manuscript Received: 22 April 2025
1st Manuscript Revision Received: 12 August 2025
2nd Manuscript Revision Received: 8 November 2025
Accepted Manuscript: 22 July 2026